PAPER • OPEN ACCESS

Determination of thermoelectric properties from micro four-point probe measurements

To cite this article: Benny Guralnik *et al* 2022 *Meas. Sci. Technol.* **33** 125001

View the article online for updates and enhancements.

Determination of thermoelectric properties from micro four-point probe measurements

Benny Guralnik[1,2,*] , **Ole Hansen**[2] , **Andreas R Stilling-Andersen**[2] ,
Søren E Hansen[2] , **Kasper A Borup**[3] , **Besira M Mihiretie**[4] ,
Braulio Beltrán-Pitarch[1,2] , **Henrik H Henrichsen**[1], **Rong Lin**[1], **Lior Shiv**[1],
Bo B Iversen[3] , **Peter F Nielsen**[1] **and Dirch H Petersen**[2]

[1] CAPRES—a KLA company, Diplomvej 373, 2800 Kgs. Lyngby, Denmark
[2] Technical University of Denmark, DK-2800 Kgs. Lyngby, Denmark
[3] Department of Chemistry, Aarhus University, Langelandsgade 140, DK-8000 Aarhus C, Denmark
[4] Hot Disk AB, SE-41288 Gothenburg, Sweden

E-mail: benny.guralnik@gmail.com

Abstract

Micro four-point probing is a branch of electrical metrology where electrical (and electromagnetic) properties of charge carriers such as conductance, mobility, and tunneling magnetoresistance can be accurately and precisely determined at the μm scale and below. Here, we propose and demonstrate a novel application of micro four-point probe (M4PP) aimed at quantifying the thermoelectric properties of a sample. Specifically, we show that for an AC current passing through a bulk material at a low angular frequency ω, the voltage drop across the sensing electrodes at 2ω is to first order proportional to the ratio (α/κ) of its Seebeck coefficient (α) to its thermal conductivity (κ). Verified by numerical simulations, our analytic theory is then put into practice on a suite of p- and n-type bulk semiconductors (Si, Ge, and BiTe). The M4PP estimates of the Seebeck coefficient in these materials are characterized both by high accuracy and precision, suggesting a novel *in-situ* metrology of thermoelectric properties at the μm scale.

Keywords: micro four-point probe, Seebeck coefficient, 2ω method, self-heating effect

(Some figures may appear in colour only in the online journal)

1. Introduction

A key challenge in keeping up with Moore's law is the overheating of nanoscale electronic devices, which is increasingly exacerbated as device sizes approach the mean free paths (MFPs) of electrons and phonons [1]. To regulate the operating temperature in such devices, an ever-growing focus is set on both describing and engineering the interplay between three key thermoelectric properties [2], namely the electrical conductivity (σ), thermal conductivity (κ), and the Seebeck coefficient (α). The importance of this triad (which, alongside the temperature T, comprise the thermoelectric figure-of-merit $ZT = \sigma\alpha^2 T/\kappa$) reaches far beyond thermal energy conversion, and is arguably at the crux of current technological progress [3]. This is so because thermal budgets of devices have a direct effect on their efficiency, reliability, and lifespan; even a suboptimal combination of the thermoelectric properties, or their unwarranted spatial variation, can result in device thermal failure, memory cell resetting, faulty logic operations, etc [4, 5].

Of the methods available for the characterization of electrical conductivity σ on the microscale, the micro four-point

probe (M4PP) technique is a well-established metrology requiring only a brief and arguably non-destructive contact between several miniature electrodes (e.g. figure 1(a)) with the surface of the sample [6]. Alongside the standardization of M4PP over the past decades [7], comparable metrologies (in terms of spatial resolution, accuracy, and precision) have also emerged for the determination of the Seebeck coefficient [8] and of thermal conductivity [9]. To date, the two latter techniques have a narrower *in-situ* applicability (e.g. imposing constraints on the continuity and layering of the probed materials [10]), while involving a more elaborated experimental setup (e.g. multiple cross-calibrations with reference materials [9]). Thus, a continued improvement of each of the above methods, as well as any potential methodological crossovers, are of high technological and societal value.

Within the field of electrical probing, self-heating effects (SHE) can generally be understood as electrical measurement artefacts related to the probing methodology itself, resulting in biased estimates of the sought electromagnetic properties [11, 12]. In materials which exhibit measurable thermoelectrical effects, SHE can be ascribed to at least three interrelated phenomena, in which σ, κ, and α are tightly intertwined as follows [13]:

(a) Joule heating, in which passage of an electric current of density j through a conductor of resistivity $\varrho = \sigma^{-1}$ dissipates the power density $P = j^2/\sigma$, thereby affecting the proximal temperature via $P/T = R_\theta(\kappa,...)$, where R_θ is the system's thermal resistance (itself inversely proportional to the thermal conductivity κ).

(b) Temperature-dependence of $\sigma(T)$ and $\kappa(T)$, implying a constant feedback between σ and κ being locally affected by the dissipation of Joule heat, and the amount of Joule heat generated in turn.

(c) Thermoelectric voltage, reaching $\nabla V = -\alpha \nabla T$ at steady state, in thermoelectric materials subject to a non-uniform temperature distribution. This additional voltage affects j and thereby P, creating an additional heat flux due to the Peltier and Thomson effects (see section 2), and thus indirectly influencing (a) and (b).

While these effects are often negligible under macroscale four-terminal sensing, recent numerical simulations suggested potential offsets of up to 40% in thermoelectric materials when four-terminal probed with DC on the mm scale [14]. Extending such simulations to the μm scale, it is easy to show that if probed with DC, M4PP measurements of a typical thermoelectric material may results in conductivity estimates that are off by a whole order-of-magnitude.

Recently it has been shown that a limited combination of SHE phenomena above (a, and a subset of b) may be quantified by M4PP [15], and further compensated for by lock-in amplification (LIA) measurements made at low AC frequencies $I = I_0 \sin(\omega t)$ [16]. Specifically, it has been shown that the magnitude of SHE arising from Joule heat under a linearized $\Delta\varrho \propto \Delta T$ regime (a first-order temperature coefficient of resistance, TCR) is mirrored in both the 1ω and 3ω

voltages, in a way that enables a linear combination of the two that eliminates the SHE contribution altogether. These studies also demonstrated that the 1ω and 3ω voltages can be utilised to characterize the TCR of the material, if its geometry, and the thermoelectric parameters σ, κ, and α, are independently known. In the present work, we target the 2ω voltage, and utilize it for the determination of the α/κ ratio.

Specifically, we demonstrate that during M4PP measurements in thermoelectric materials, Joule and Peltier heating in the vicinity of the current-conducting electrodes may result in considerable temperature differences (up to ∼1 K) across the voltage-sensing terminals. These gradients can be accurately predicted by a combination of analytical theory and experimental data (two-point transfer resistance measurements). We show that at AC frequencies sufficiently low to avoid either a thermal lag, or an electrostatic disequilibrium, the 2ω voltage can be measured with high repeatability and precision, and is proportional to the material's α/κ ratio. Together with the 1ω voltage (translatable to σ), our presented methodology is the first M4PP application addressing all three thermoelectric parameters (σ, κ and α) from a single μm-scale electric measurement.

2. Theory

In the absence of an external magnetic field, and negligible internal magnetic fields due to induction, the rate of heat evolution per volume $\dot{Q}$ in a homogeneous conductor is [13, 17]:

$$\dot{Q} = \frac{j^2}{\sigma} + \nabla \cdot (\kappa \nabla T) - T\mathbf{j} \cdot \nabla\alpha, \qquad (1)$$

where $j = |\mathbf{j}|$ is the (norm of) electric current density, σ and κ are coefficients of electrical and thermal conductivity, T is temperature, and α the Seebeck coefficient. The first r.h.s. term j^2/σ discloses electrical work production and dissipation (Joule heat). The change in thermal conduction due to heat produced or absorbed is given by $\nabla \cdot (\kappa \nabla T)$. The final term $-T\mathbf{j} \cdot \nabla\alpha$ is separable [13] into two contributions $\mathbf{j} \cdot (\nabla\Pi - \alpha\nabla T)$, of which the first is pure Peltier heat (further affected by a spatial gradient in the Peltier coefficient $\Pi = \alpha T$), and the second is the pure Thomson effect (heat production driven solely by a thermal gradient ∇T).

To solve equation (1), we consider a thermal steady-state $\dot{Q} = 0$ [13], and further assume $\nabla\kappa \cong 0$ and $\nabla\alpha \cong 0$, which simplifies the differential equation to $\kappa \nabla^2 T = -j^2/\sigma$ [see 18, 19]. While M4PP sampling involves no internal heat production whatsoever ($Q = 0$) [17], the more generalized assumption of $\dot{Q} = 0$ leads to exactly the same result [13]. The neglection of the spatial gradients in κ and α are warranted by the fact, that the Joule heating is extremely localized at the vicinity of the M4PP contacts (with power density being proportional to r^{-4}; see equation (2) below), while the temperature dependencies $\kappa \sim 1/T$ and $\alpha \sim \ln(T)$ in the materials under test are insubstantial under the typically modest heating (tens of degrees K; see [15]) that M4PP probing
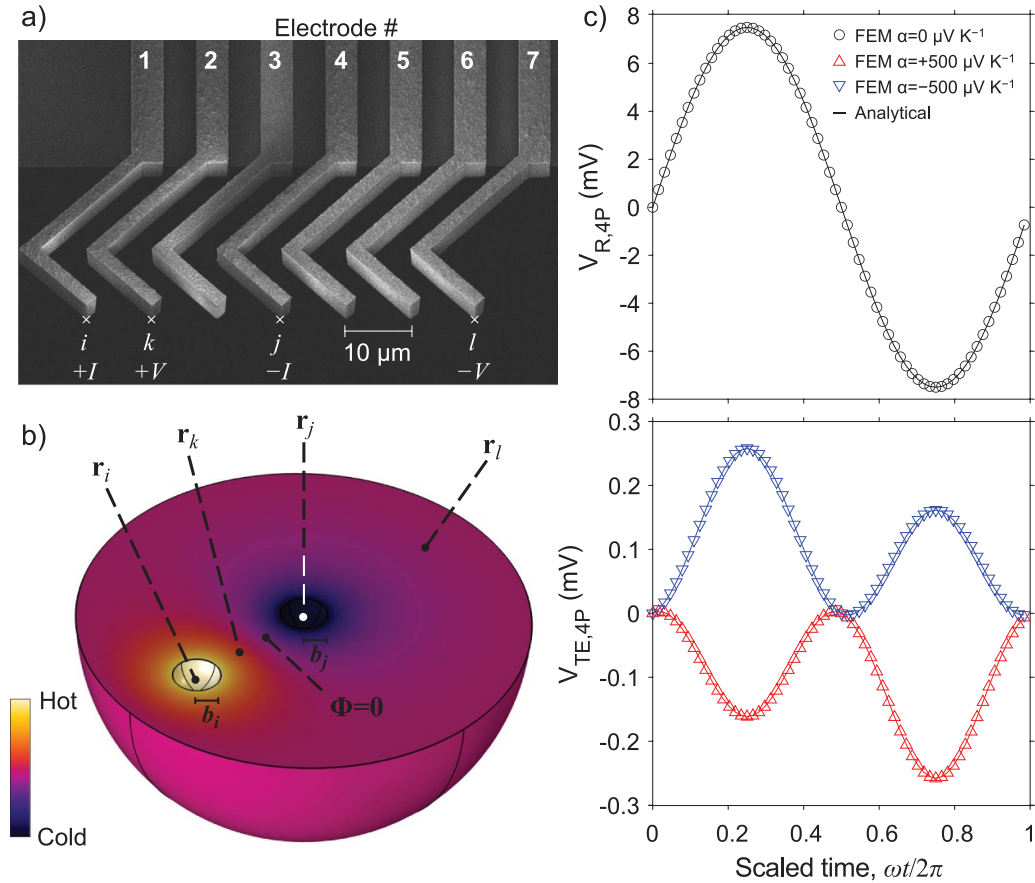
Figure 1. (a) Scanning electron microscope image of the Hall probe (L7PP) used in this study, with electrode connectors labelled 1 through 7. Although arbitrary, the marked terminal assignments of current ($+I$, $-I$) and voltage ($+V$, $-V$) are further simulated in (b), (c). (b) Schematic (not to scale) of the finite element model, including a hemispherical domain with a reference potential point, two hemispherical indentations representing current source and drain, and two points representing voltage pick-up terminals. Color corresponds to the domain temperature at $t = \pi/2\omega$, arising from Joule heating and thermoelectric effects. (c) The simulated (symbols) and analytical (lines) potential difference across the voltage probes for an undoped, p-type, and n-type materials, decomposed to its resistive contribution V_R (top panel) and the thermoelectric contribution V_{TE} (bottom panel).

exerts. These assumptions, as well as all subsequent steps of the derivation, have been further verified against a numerical simulation (figure 1(c) and section 4.1).

To represent a M4PP sample, we consider a thermally insulated half space substrate ($z < 0$), with a small indented hemisphere of a radius b at the origin [20], representing an electrode-substrate contact. The surface of this contact acts as a single electrical terminal, injecting a hemispherically symmetric current density $\mathbf{j} = (I/2\pi r^2)\hat{\mathbf{r}}$ into the substrate (with ground infinitely far away). Following these assumptions, equation (1) can be recast as:

$$\frac{1}{r^2}\frac{\partial T}{\partial r}\left(r^2\frac{\partial T}{\partial r}\right) = -\frac{I^2}{4\pi^2\sigma\kappa r^4}, \quad (2)$$

subject to the boundary conditions:

$$\begin{aligned} T(r \to \infty) &= T_0, \\ \kappa\nabla T(b) &= \alpha T(b)j(b), \end{aligned} \quad (3)$$

of which the first fixes the undisturbed temperature infinitely far away from the contact, and the second applies Peltier heat at the electrode-substrate interface. It may be shown that equations (2) and (3) are satisfied by:

$$\begin{aligned} T(r) = T_0 + \frac{1}{2\pi\kappa r}&\left\{\frac{I^2}{4\pi\sigma b}\left[1 - \frac{b}{r} + \left(1 + \frac{\alpha I}{2\pi\kappa b}\right)^{-1}\right] \right. \\ &\left. - T_0\alpha I\left(1 + \frac{\alpha I}{2\pi\kappa b}\right)^{-1}\right\} \end{aligned}, \quad (4)$$

where $r = |\mathbf{r}|$, $r > b$ is the norm of an arbitrary location vector $\mathbf{r}$ outside of the contact. To isolate the temperature change, we introduce $\Delta T(r) = T(r) - T_0$. Since for a typical M4PP measurement one may expect $\alpha I/2\pi\kappa b << 1$, equation (4) can be simplified via a first-order Taylor series approximation $\left(1 + \frac{\alpha I}{2\pi\kappa b}\right)^{-1} \cong 1 - \frac{\alpha I}{2\pi\kappa b}$. This simplification, under further substitution of a low-frequency (pseudo-DC) sinusoidal current $I = I_0\sin(\omega t)$, rearrangement by increasing harmonic components, and a convenient parametrization for later use, results in:

$$\Delta T(\mathbf{r},b,I_0) \cong \frac{I_0^2}{4\pi\kappa|\mathbf{r}|}\left(\frac{1-\frac{b}{2|\mathbf{r}|}}{2\pi\sigma b} + \frac{T_0\alpha^2}{2\pi\kappa b}\right)$$
$$+ \frac{I_0}{2\pi\kappa|\mathbf{r}|}\left[T_0\alpha + \frac{3}{4}I_0^2\left(\frac{\alpha}{2\pi\kappa b}\frac{1}{4\pi\sigma b}\right)\right]\sin(\omega t+\pi)$$
$$+ \frac{I_0^2}{4\pi\kappa|\mathbf{r}|}\left(\frac{1-\frac{b}{2|\mathbf{r}|}}{2\pi\sigma b} + \frac{T_0\alpha^2}{2\pi\kappa b}\right)\sin(2\omega t-\pi/2)$$
$$+ \frac{I_0^3}{8\pi\kappa|\mathbf{r}|}\left(\frac{\alpha}{2\pi\kappa b}\frac{1}{4\pi\sigma b}\right)\sin(3\omega t). \qquad (5)$$

To describe the total electric potential Φ at $\mathbf{r}$ (granted $|\mathbf{r}| > b$), we sum up the resistive component $\Phi_R = I_0\sin(\omega t)/2\pi\sigma r$ [21], with the thermoelectric component $\Phi_{TE} = -\alpha\Delta T$ [22]:

$$\Phi(\mathbf{r},b,I_0) = \Phi_R(\mathbf{r},b,I_0) + \Phi_{TE}(\mathbf{r},b,I_0)$$
$$= \frac{I_0\sin(\omega t)}{2\pi\sigma|\mathbf{r}|} - \alpha\Delta T(\mathbf{r},b,I_0). \qquad (6)$$

The potential drop across the voltage probes in a four-point resistivity measurement can be approximated via a linear combination of four instances of equation (6) as follows (figure 1(b)). Let $\mathbf{r}_i$ and $\mathbf{r}_j$ be the locations of current sources $+I_0$ and $-I_0$, respectively, and $\mathbf{r}_k$ and $\mathbf{r}_l$ the locations of voltage probes of polarity $+V$ and $-V$. By superposition of the electric potentials from both sources, and taking the potential difference across probes k and l, the four-point voltage V_{4P} is given by [21]:

$$V_{4P} = V_{R,4P} + V_{TE,4P}$$
$$= \Phi(\mathbf{r}_i - \mathbf{r}_k, b_i, I_0) + \Phi(\mathbf{r}_j - \mathbf{r}_k, b_j, -I_0)$$
$$- \Phi(\mathbf{r}_i - \mathbf{r}_l, b_i, I_0) - \Phi(\mathbf{r}_j - \mathbf{r}_l, b_j, -I_0), \qquad (7)$$

where b_i and b_j are the hemispherical contact radii of the current source and drain. Equation (7) may be expected to be accurate as long as the norms of the vector terms significantly exceed $\max(b_i, b_j)$.

3. Methods and materials

3.1. Numerical simulations

The accuracy of equation (4) was verified using symbolic integration of equations (2) and (3) in MATLAB Symbolic Math Toolbox® [23]. Further approximation errors due to the Taylor-series expansion (equation (5)), and source superposition (equation (7)), were studied by generating synthetic datasets, whose voltage was decomposed using a numerical LIA, and cross-checked against a fast Fourier transform. Finite element method simulations were undertaken in COMSOL Multiphysics® [24], using coupled modules of electric currents, heat transfer in solids, and thermoelectric effects. Figure 1(b) shows a not-to-scale sketch of the model, including a sample represented by a large hemisphere, with a thermally insulated top surface. The hemispherical sample extends two orders of magnitude beyond the M4PP footprint, at which we impose an isothermal boundary condition with $T_0 = 300$ K. Two current terminals of opposite polarity were represented by two tightly meshed hemispherical indentations of radius b_i

and b_j into the top surface; the voltage terminals were represented by a surface mesh point each; the electric potential was kept at zero at an arbitrary but convenient reference point (the geometric average of all terminal locations). The time dependent electric potential due to the low-frequency sinusoidal AC current passed between the current terminals at an angular frequency $\omega = 2\pi f$ was sampled and used as input in the digital LIA.

3.2. Samples

In this study we obtained and studied $N = 10$ bulk thermoelectric materials (table 1), further divided into $N = 5$ calibration samples (on which M4PP protocols were developed), and $N = 5$ test samples (representing challenging materials with further unknowns). The physical sample dimensions were all >1.5 orders of magnitude larger than the largest mean electrode pitch (20 µm) of the selected M4PP, satisfying the semi-infinite substrate per the derivations in equations (1) through (7).

The calibration samples (lab codes 4790, 4791, 785, 1113, and 2167) comprised of single-crystal, Czochralski-grown, uniformly doped, industrial-grade, p- and n-type bulk Si wafers (Ø = 100 mm, 0.50–0.55 mm thick) bought from commercial suppliers (Okmetic and UniversityWafer). Reference (independent) values of κ and α for the calibration samples were obtained as briefly outlined next. Thermal conductivity κ_{ref} was measured using the transient planar source (TPS) method [29], on a Hot Disk TPS-3500 system (ISO22007-2) under the assumptions of thin slab geometry and transient response [30, 31]. The offset-free [32] Seebeck coefficients α_{ref} were obtained using the slope method [33] on a custom-built apparatus replicating that of Iwanaga *et al* [34] and measuring under a modified four-point geometry [35]. All macro-scale reference values reported in table 1, are associated with standard errors of the mean of 2.5%.

The challenging samples included two industrial-grade Ge wafers bought from UniversityWafer (lab codes 2575, 2477), an unpolished Si:As wafer provided by Topsil GlobalWafers A/S (lab code 2875), and two in-house heat-pressed polycrystalline BiTe ingots (lab codes TEP0, TEN0). The Seebeck coefficients of these samples were characterized as above, while their κ_{ref} were calculated from theory [25–27, 35] due to small and irregular sample size that precluded reproducible TPS measurements.

The Seebeck coefficient of the M4PP probe ($\alpha_{probe} = -19.8$ µV K^{-1}) was measured on a macroscale split sample from M4PP production, matching standard literature values for bulk Ni.

3.3. Micro four-point probe measurements

Electric resistance measurements were performed using a CAPRES microRSP®-A300 tool, using an extended digital LIA module [16], which logs the two- and four-point transfer resistance $R_{n\omega}$ and its phase $\varphi_{n\omega}$ up to the third harmonic ($n = 1, 2, 3$) of the input current frequency. All samples were characterized using a low frequency current $I = I_0\sin(\omega t) =$

Table 1. Sample description, macroscale reference values, and the best-fit M4PP results.

Sample				Macroscale		M4PP			
Subset	Lab code	Type	Material	$\alpha_{\rm ref}$ (μV K^{-1})	$\kappa_{\rm ref}$ (W m^{-1} K^{-1})	ϱ (Ω μm)		$\alpha_{\rm M4PP}$ (μV K^{-1})	
Calibration	4790	P	Si:B	632	128	132.5	$\pm$0.08	639	$\pm$3
	4791	P	Si:B	578	126	107.0	$\pm$0.03	578	$\pm$4
	785	P	Si:B	251	65	12.8	$\pm$0.01	267	$\pm$1
	1113	N	Si:As	-310	84	26.9	$\pm$0.02	-298	$\pm$2
	2167	N	Si:P	-349	111	31.1	$\pm$0.03	-325	$\pm$3
Test	2875	N	Si:As	-435	111[a]	45.9	$\pm$0.15	-432	$\pm$12
	2575	P	Ge:Ga	540	58[b]	554.9	$\pm$0.50	560	$\pm$41
	2477	N	Ge:Sb	-662	58[b]	Fermi-level pinning			
	TEP0	P	Bi$_{0.3}$Sb$_{1.7}$Te$_3$	115	1.8[c]	14.6	$\pm$0.10	89	$\pm$2
	TEN0	N	Bi$_2$Te$_{2.7}$Se$_{0.3}$	-130	1.5[d]	20.5	$\pm$0.19	-89	$\pm$2

The thermal conductivities of the test samples have been calculated/estimated from literature after [a]Lee and Hwang [25], [b]Ohishi *et al* [26], [c]Wang *et al* [27], and [d]Hu *et al* [28].

$\sqrt{2}I_{\rm rms}\sin(2\pi ft)$ with $f = 12.06$ Hz, using an M4PP with seven equidistant electrodes (figure 1(a)). This probe comprises of 2.3 μm wide L-shaped silicon cantilevers, uniformly spaced 10 μm apart, and having one side coated with Ni [36]. The electrical measurements included 158 four-point configurations, sampling all unique four-point sub-probes (7!/4!(7−4)! = 35), between two and eight times each (favouring configurations that maximize the signal of interest, $V_{\rm 4P,2\omega}$). Ten sets of 158 configurations were measured for seven different r.m.s. currents $I_{\rm rms}$, varied in the range 0.5–5 mA, with some repeated for monitoring reproducibility. Measurements were discarded from data fitting if the first harmonic phase shift $\varphi_{1\omega}$ exceeded $0° \pm 1°$, and/or the second harmonic phase $\varphi_{2\omega}$ exceeded $\pm90° \pm 2°$, albeit these data are often in accord with their best-fit prediction (cf figure 2).

The experimental data was fitted for each current separately, as follows. At the first step, the filtered four-point, first harmonic resistance data $R_{\rm 4P,1\omega}$, governed by:

$$R_{\rm 4P,1\omega} = \frac{\varrho}{2\pi}\left(\frac{1}{|\mathbf{r}_i - \mathbf{r}_k|} + \frac{1}{|\mathbf{r}_j - \mathbf{r}_l|} - \frac{1}{|\mathbf{r}_i - \mathbf{r}_l|} - \frac{1}{|\mathbf{r}_j - \mathbf{r}_k|}\right),$$ (8)

[20] were simultaneously fitted to regress the bulk resistivity ϱ, and the inner electrode in-line positions $\mathbf{r}_2$ through $\mathbf{r}_6$ [37], with $\mathbf{r}_1$ and $\mathbf{r}_7$ fixed to their nominal positions.

At the second step, and with ϱ fixed to its best-fit value from the previous step, the two-point, first harmonic, load resistance data $R_{\rm 2P,1\omega}$, governed by:

$$R_{\rm 2P,1\omega} = \frac{\varrho}{2\pi}\left[\left(\frac{1}{b_i} - \frac{1}{|\mathbf{r}_i - \mathbf{r}_j| - b_i}\right) + \left(\frac{1}{b_j} - \frac{1}{|\mathbf{r}_i - \mathbf{r}_j| - b_j}\right)\right],$$ (9)

[see 38] were simultaneously fitted to regress contact radii b_1 through b_7. Prior to the fit, the lead resistances of the electrodes, periodically monitored for drift on a thick Ni film, were subtracted from $R_{\rm 2P,1\omega}$ [39].

At the final step, all the previously fitted parameters (ϱ, $\mathbf{r}_2$ through $\mathbf{r}_6$, and b_1 through b_7) were fixed, and the filtered,

four-point, second harmonic voltage data $V_{\rm 4P,2\omega}$ were simultaneously fitted to determine the thermoelectric properties. In the simplified approach which demonstrates the dominant proportionality between $V_{\rm 4P,2\omega}$ and α/κ, we neglected the α^2 term in equation (5), which enables us to fit the α/κ ratio directly:

$$V_{\rm 4P,2\omega} = -\frac{\alpha}{\kappa}\frac{I_0^2}{4\pi}\left(\frac{1 - \frac{b_i}{2|\mathbf{r}_i - \mathbf{r}_k|}}{2\pi\sigma b_i |\mathbf{r}_i - \mathbf{r}_k|} + \frac{1 - \frac{b_j}{2|\mathbf{r}_j - \mathbf{r}_k|}}{2\pi\sigma b_j |\mathbf{r}_j - \mathbf{r}_k|}\right.$$
$$\left. - \frac{1 - \frac{b_i}{2|\mathbf{r}_i - \mathbf{r}_l|}}{2\pi\sigma b_i |\mathbf{r}_i - \mathbf{r}_l|} - \frac{1 - \frac{b_j}{2|\mathbf{r}_j - \mathbf{r}_l|}}{2\pi\sigma b_j |\mathbf{r}_j - \mathbf{r}_l|}\right),$$ (10)

comparing equation (10) with experimental quantities via:

$$R_{\rm 4P,2\omega} = |V_{\rm 4P,2\omega}|/I_0,$$ (11)

$$\varphi_{\rm 4P,2\omega} = -\pi/2 \cdot {\rm sgn}(V_{\rm 4P,2\omega}).$$ (12)

In the more accurate approach, accounting for the Seebeck voltage contribution from the probe itself, the M4PP Seebeck coefficients $\alpha_{\rm M4PP}$ (table 1) were obtained by fitting data with the full equations (5)–(7), with κ fixed to its macroscale reference value $\kappa_{\rm ref}$ (table 1), and the probe's own Seebeck coefficient substracted via $\alpha = \alpha_{\rm M4PP} - \alpha_{\rm probe}$.

4. Results

4.1. Theory validation

Having verified the exact solution (equation (4) via symbolic integration of equations (2) and (3)), the accuracy of the approximation equation (5) was further evaluated against equation (4) via numerical lock-in of synthetic data, generated by equations (4) and (5) for a characteristic target material (doped silicon with $\sigma = 10^{-4}$ Ω m, $\kappa = 120$ W m^{-1} K^{-1}, and $\alpha = \pm500$ μV K^{-1}) and typical M4PP settings ($r = 10$ μm, $b = 250$ nm, $I_{\rm rms} = 5$ mA and $T_0 = 300$ K). Under these conditions, the relative error of the obtained amplitudes for $V_{1\omega}$ and
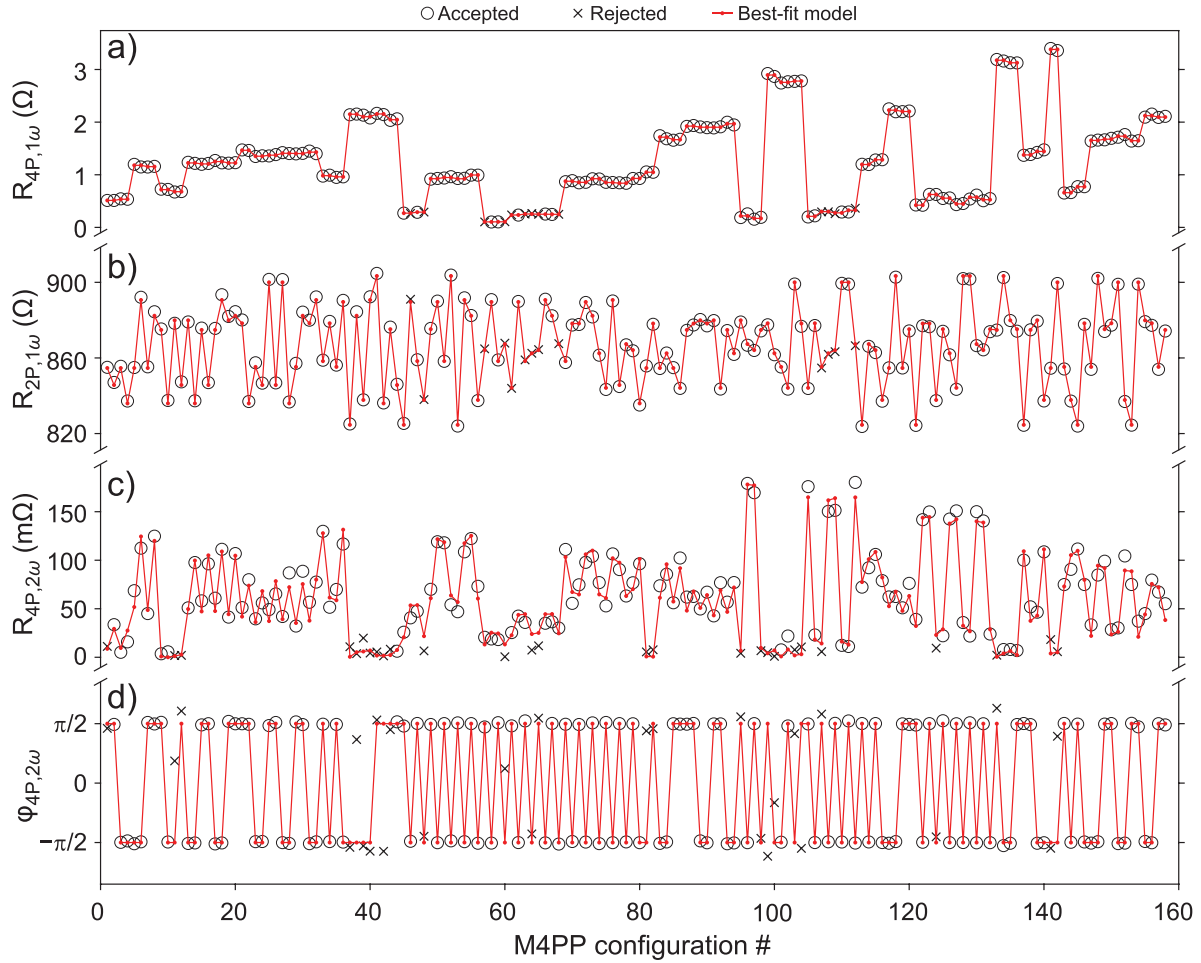
Figure 2. Accepted (circles) and rejected (crosses) M4PP data for sample 4790 measured at $I_{rms} = 4.08$ mA, alongside the best-fit model prediction from equations (8)–(12) (lines). (a) Four-point first harmonic resistance, (b) two-point first harmonic resistance, (c), (d) four-point second harmonic resistance amplitude (c) and phase (d). The coefficient of determination (R2) is in excess of 0.95 for all the four datasets (see figure 3(a)); all fitting parameters are further shown in figures 3(b)–(d). The order of measurements (the *x*-axis) has been optimised for reproducibility.

$V_{2\omega}$ is 0.02% on average (with zero error on V_{DC}, and 1.3% on $V_{3\omega}$), percieved as sufficiently accurate for the incorporation of equation (5) in equations (6) and (7).

To test the accuracy of the source superposition approximation in equations (6) and (7) to predict four-point resistance data, a time-dependent finite element model (FEM) was run for $f = 12$ Hz and the same parameters as above, with current terminals $+I$ at $\mathbf{r}_i = [-30, 0]$ and $-I$ at $\mathbf{r}_j = [0, 0]$, and voltage terminals $+V$ at $\mathbf{r}_k = [-20, 0]$ and $-V$ at $\mathbf{r}_l = [30, 0]$ (all coordinates in μm). Figure 1(b) is a not-to-scale sketch of the FEM simulation, while figure 1(c) shows the resistive (top panel) and thermoelectric (bottom panel) components of voltage, as simulated numerically (symbols in figure 1(c)) and approximated analytically via equations (5)–(7) (lines in figure 1(c)). The amplitudes and phases obtained via numerical LIA of FEM-simulated voltage, coincided with amplitudes and phases as predicted by equations (5)–(7) to within 0.8% on average, with the second harmonic resistance $R_{2\omega}$ showing an offset of only <0.3%. Recognizing that the accuracy of FEM is limited by mesh quality and numerical tolerance, while equations (5)–(7) are merely an approximation, the high

degree (>99%) to which these two approaches agree is noteworthy (the sub-percent mismatch is of the order of magnitude of M4PP precision [37]).

As a final step, we conducted FEM simulations with α ranging 0.1–1 mV K^{-1}, converted the resultant voltage to harmonic amplitudes and phases by LIA, and fitted equations (5)–(7) with α as the fitting parameter. Initial analysis, utilizing equations (10)–(12) where the α^2 term is neglected, resulted in α estimates off by up to ~8%; direct fitting of equations (5)–(7) yielded far more accurate values of α, offset by ~2% at most. Following the latter rigorous testing, we deem equations (5)–(7) suitable for the analysis of experimental data.

4.2. Data reduction

Figure 2 shows the experimental data for sample 4790, as measured at an $I_{rms} = I_0/\sqrt{2}$ current of 4.08 mA. The order of measurements in figure 2 (the *x*-axis) is heuristic, in the sense that the number of four-point configurations, as well as their particular order, are subject of choice and optimization by the practitioner. After extensive testing, the particular sequence
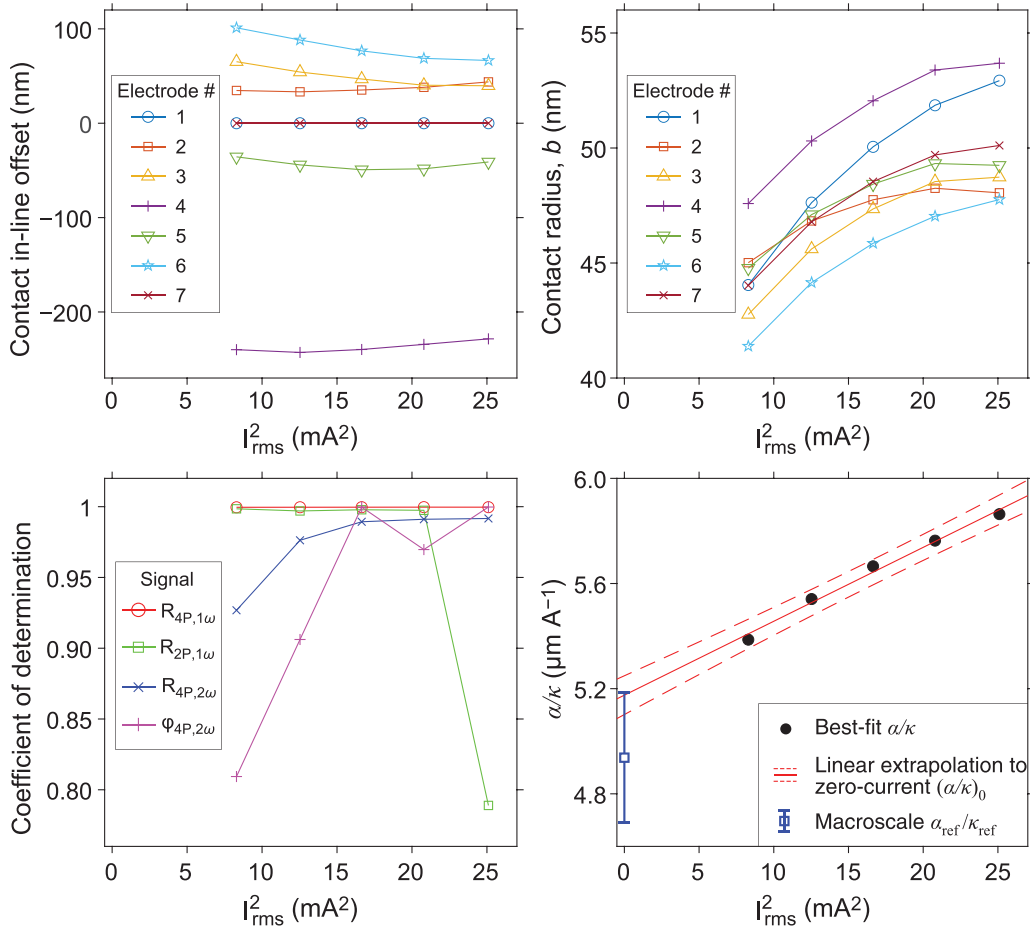
Figure 3. Summary of fitting results for sample 4790, plotted against current squared. (a) Coefficients of determination. (b) Best-fit electrode positions from equation (8), expressed as Euclidean distance from the probe's nominal positions $|\mathbf{r}_{x,\text{nominal}} - \mathbf{r}_{x,\text{best-fit}}|$. (c) Best-fit contact radii from equation (9). (d) Best-fit α/κ ratio from equation (10); the linear trend in the latter data may be extrapolated to zero current (red lines), retrieving TCR-unaffected intercept which within uncertainties overlaps with the independent estimate $\alpha_{\text{ref}}/\kappa_{\text{ref}}$ (see text for discussion).

shown in figure 2 was adopted after it was found to improve reproducibility to <2.5% (relative standard error of the mean) across different probe engages. The symbols in panels (a)–(d) correspond to experimental data, namely the amplitudes of the first harmonic four-point $R_{4P,1\omega}$ (a) and two-point $R_{2P,1\omega}$ (b) resistances, and the amplitude $R_{4P,2\omega}$ (c) and phase $\varphi_{4P,2\omega}$ (d) of the second harmonic four-point resistance. Note that the corresponding phases of $R_{4P,1\omega}$ and $R_{2P,1\omega}$ are negligibly different from 0° and are thus not shown. These data were collected and fitted as described in section 3.3, with $R_{4P,1\omega}$ being fitted first to obtain resistivity, $R_{2P,1\omega}$ second to obtain contact radii, and finally $R_{4P,2\omega}$ to obtain α/κ. The coefficient of determination (r^2) for the fits in figure 2, alongside all the fitting parameters, are shown in figures 3(a)–(d), respectively, alongside fitting results for several other currents. Measurements at currents $I_{\text{rms}} < 2.9$ mA yielding clearly anomalous $R_{4P,2\omega}$ data, and abnormally low $r^2 < 0.9$ for the best-fit models, have been discarded from the zero-current extrapolation of the thermoelectric parameters (see section 5), as described next.

For all samples, the accepted best-fit α/κ ratios trend linearly with current squared (e.g. figure 3(d)), strongly suggesting a TCR effect in play [11, 12]. The theoretical TCR

values for the calibration samples vary across an order of magnitude (in the range $0.2–2 \times 10^{-3}$ K^{-1}) and were confirmed experimentally via hotplate measurements of $\varrho(T)$ in the 15 °C–55 °C range. Initially, a 3ω correction to the transfer resistance data has been considered [11]. However, in the case of a material with a combination of prominent TCR and thermoelectric effects, it is logical to expect that the 3ω signal ($R_{3\omega}$) will contain a mixture of a TCR contribution [11] and a Peltier heat contribution (equation (5)), at a ratio which is difficult to predict analytically [17]. Thus, a standard 3ω correction [11] of e.g. $R_{2P,1\omega}$ data (critical for the determination of the correct amount of heat produced at the contacts) would partially remove the thermoelectric heating effect that we are interested in quantify in the first place. Therefore, we adopted the zero-current extrapolation approach, which is widespread in electrical metrology for detrending TCR effects [11, 12]. The extrapolation of data in figure 3(d) to zero current yields $(\alpha/\kappa)_0 = 5.18 \pm 0.03$ μm A^{-1}, which is within error of its reference estimate $\alpha_{\text{ref}}/\kappa_{\text{ref}} = 4.93 \pm 0.25$ μm A^{-1}.

The aforementioned $(\alpha/\kappa)_0$ estimate neglects secondary effects proportional to α^2, and further suffers from a voltage offset due to the probe's own Seebeck coefficient, proportional
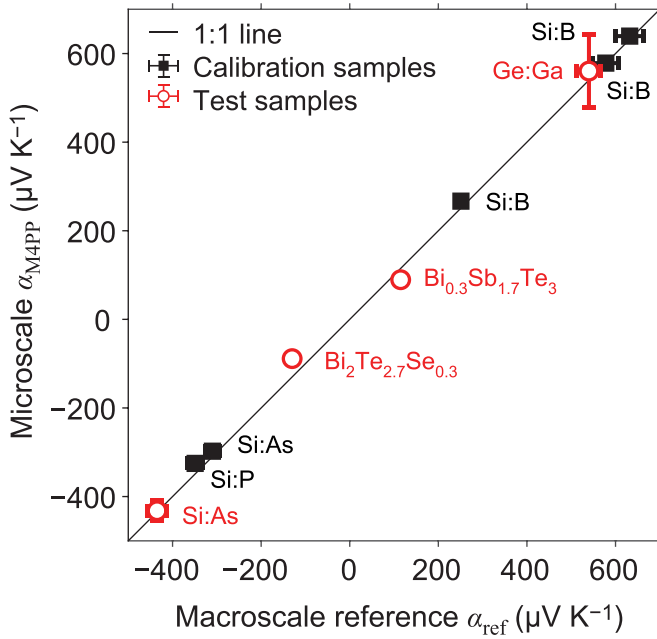
Figure 4. Comparison of the best-fit M4PP estimates of the Seebeck coefficient against their independent reference values.

to α_{probe}/κ, and thus differentially affecting samples with varying thermal conductivity. In fact, the offset magnitude ($\sim$5%) between the best-fit M4PP $(\alpha/\kappa)_0$ and its independent reference value $\alpha_{ref}/\kappa_{ref}$ is fully expectable from our sensitivity analysis where the effect of dropping the α^2 term was tested (see section 4.1). To demonstrate that our methodologically most accurate estimates of thermoelectric parameters match their reference values within an even smaller error, we used the full equations (5)–(7) to fit the data (e.g. figure 2) for each sample, with κ fixed to its macroscale reference value, and α_{M4PP} as the only unknown (where the apparent Seebeck coefficient $\alpha = \alpha_{M4PP} - \alpha_{probe}$ accounts for contributions from both the sample and the probe). These M4PP estimates of the Seebeck coefficient (table 1) are plotted against their corresponding reference values in figure 4.

5. Discussion and conclusions

For all the $N = 5$ calibration samples, our methodologically most accurate α_{M4PP} estimates (table 1) are all within error of their independent macroscale estimates (figure 4); so are two of three single-crystal test materials (Si:As and Ge:Ga), the third (Ge:Sb) considered unmeasurable due to a strong Fermi-level pinning [40] that yielded highly rectified spurious signals, none of which could be plausibly fitted by the model considered here (equations (8)–(12)).

M4PP measurements on the p- and n-type bismuth telluride ingots exhibited a considerable scatter (low reproducibility across engages), and were often characterized by a non-3D current transport [see 41]. The anisotropic behaviour of BiTe crystals is well-documented [42], while visible crystal sizes in our BiTe samples were 1–10 μm, making it likely

for M4PP probing to conduct current through multiple crystals at once. While our best estimates of the Seebeck coefficient for the BiTe ingots appear 20%–30% off their literature values (table 1), both the Seebeck coefficient and thermal conductivity can vary by a factor 2–3 between thermoelectric properties measured in parallel vs. perpendicular to the ingot pressing direction [42]. Thus, the macroscale reference values measured/estimated for these ingots (table 1) have the polycrystallinity effect all averaged out, while the M4PP measurements are likely to have been highly affected by the orientation of the microcrystal aggregates that the current was conducted through.

The problem of probe offset is not unique to M4PP, as the value of the measured Seebeck coefficient of semiconductors does weakly vary with the work function of the metallic leads that probe it [e.g. 43]. While the unwanted thermoelectric contribution from the Ni leads is relatively low (-19.8 μV K^{-1}), the actual voltage offset scales this value by the sample's thermal conductivity (cf equation (10)), thus making α_{probe} inseparable from sample properties. Optimization of future microprobes, e.g. through the use of platinum coating to bring the absolute Seebeck coefficient of the probe close to zero, or via maximizing the thermal insulation of the metallization from the probe's mechanical backbone, is underway.

In our conceptual model, all the heating power is presumed to dissipate solely within the substrate, with no heat backflow into the electrodes ('cold finger effect'). To qualitatively estimate a potential cold finger offset in our samples, consider that the thermal spreading resistance into the sample is $R_{th,sp} = 1/2\pi\kappa b$, while the thermal resistance of an electrode is $R_{th,el} = (1/2\pi b + L/A)/\kappa_c$, where L, A and κ_c are the length, cross section area, and thermal conductivity of the electrode's cantilever, respectively. Taking representative values for a Si sample ($\kappa = 128$ W m^{-1} K^{-1} and $b = 50$ nm; sample 4790) and for the Ni-coated polysilicon cantilevers ($L/A = 10^7$ m^{-1} and $\kappa_c = 30$ W m^{-1} K^{-1}), the effective thermal conductivity of sample 4790 would appear offset from its true value by $R_{th,el}/R_{th,sp} = 5.7\%$. An even smaller offset $\sim$4% has been obtained through a FEM simulation, where heat is generated also within the electrode via Joule heating, further reducing the error due to the cold finger effect. Experimentally, the fact that M4PP provides Seebeck coefficient estimates that match their reference values, implies that except for the high-ZT BiTe samples, the systematic cold finger effect in the Si and Ge measurements is likely secondary to negligible ($<$5%). While a more rigorous investigation of the cold finger effect is outside the scope of the present study, we anticipate that M4PP could be further optimized to have a larger thermal resistance, e.g. through exchanging the polysilicon substrate with SiO$_2$. This would reduce the cold finger effect by more than an order of magnitude, and hopefully make the effect negligible also for high-ZT materials.

A few comments can be made with respect to the degree to which $V_{4P,2\omega}$ may be influenced by other effects than Seebeck and Peltier (both included in deriving equation (4)). Since in equation (1), the Thomson effect is proportional only to the first power of current, $V_{4P,2\omega}$ may be safely regarded as

insensitive to the Thomson effect altogether [17, 18]. Granted that ΔT at 2ω is proportional to I_{rms}^2 (equation (5)), any component of $V_{4P,2\omega}$ arising from the Seebeck effect ($\Delta V = -\alpha \Delta T$) is also expected to be proportional to I_{rms}^2 (equation (10)). At sampling currents $I_{\text{rms}} > 2.9$ mA, this proportionality $V_{4P,2\omega} \propto I_{\text{rms}}^2$ was indeed strictly obeyed (e.g. figures 2 and 3(d)). However, at $I_{\text{rms}} < 2.9$ mA, we observed an unanticipated $V_{4P,2\omega} \propto I_{\text{rms}}^m$ behaviour, where $-\infty < m \leqslant 0$. Studying the obtained I–$V_{4P,1\omega}$ and I–$V_{4P,2\omega}$ curves over the 100 µA–5 mA range, we observe a clear fingerprint of a highly non-linear, metal-semiconductor Schottky contact behaviour at the low current end. Empirically, when the same measurement protocol is applied at currents $I_{\text{rms}} < 2$ mA, we observe $V_{4P,2\omega}$ whose best-fit Seebeck model (equations (10)–(12)) is up to orders of magnitude away from the measurement points ($r^2 \sim 0$), implying that the signals are contaminated by an oscillating forward/reverse bias of the Schottky contacts at 2ω. A transitional range, where m changes sign and approaches 2 is observed 1 mA < I_{rms} < 2 mA, until at $I_{\text{rms}} > 2.5$ mA the model's coefficient of determination is acceptable ($r^2 > 0.9$) to assume signal dominance by the process described by equation (1). Since the range of currents where $V_{4P,2\omega} \propto I_{\text{rms}}^2$ is easy to experimentally identify, further investigation of the non-linear behaviour of metal-semiconductor contacts at low currents remains outside of the scope of this study.

When the heater size approaches the phonon MFP in the probed material, that material's thermal conductivity may become supressed due to ballistic heat transport, potentially causing the apparent κ to deviate from its bulk values by orders of magnitude [3, 43]. In bulk crystalline Si, the theoretical phonon MFP is 41 nm at $T = 300$ K [44], which is comparable to our best-fit contact radii b. However, ballistic transport will occur only for MFPs longer than the thermal penetration depth, which for a Joule heating frequency of $2f$ will be given by $\sqrt{D/2\pi f}$, where D is the thermal diffusivity [45]. For our experimental setup ($f = 12$ Hz) and the Si samples considered (35–68 mm^2 s^{-1}), the corresponding thermal penetration depths are 680–950 µm, four orders of magnitude longer than the prevailing MFPs. Thus, no apparent reduction of thermal conductivity due to ballistic transport should be expected [46]. While promising, the opportunity to utilize high-frequency M4PP for studying nanoscale heat transport will be considered elsewhere.

As a final cautionary note, we must stress that the presented method is currently only capable of *modelling* the temperature drop across the two voltage electrodes (cf equation (6)), while the actual temperature drop is not in any way *measured*. While for the calibration materials studied, our temperature predictions appear to be accurate, temperature fields are increasingly more difficult to model due to Joule heating in multilayered structures [15], or arbitrary nanodevice geometries [47]. Thus, for a successful application of the proposed methodology in a broader context of sample chemistries and geometries, further methodological improvements will be necessary, including independent temperature sensing on the microscale.

To the best of our knowledge, this work is the first four-terminal sensing application to simultaneously address all the thermoelectric parameters σ and α/κ from a single measurement on the microscale. Work to separate α and κ is currently underway and will be reported elsewhere. These efforts continue the methodological expansion of four-terminal sensing beyond its original use for direct sensing of electrical resistance [7; 21], and help establish M4PP as an attractive microscale technique to determine magnetoresistance [48], Hall resistance [49], and thermal properties [15, 16].

Data availability statement

The data that support the findings of this study are available upon reasonable request from the authors.

Acknowledgments

ORCID iDs

Benny Guralnik ⬤ https://orcid.org/0000-0003-3095-3868
Ole Hansen ⬤ https://orcid.org/0000-0002-6090-8323
Andreas R Stilling-Andersen ⬤ https://orcid.org/0000-0001-9847-8093
Søren E Hansen ⬤ https://orcid.org/0000-0002-3370-2389
Kasper A Borup ⬤ https://orcid.org/0000-0001-5013-6684
Besira M Mihiretie ⬤ https://orcid.org/0000-0001-8298-9462
Braulio Beltrán-Pitarch ⬤ https://orcid.org/0000-0002-4596-9582
Bo B Iversen ⬤ https://orcid.org/0000-0002-4632-1024
Peter F Nielsen ⬤ https://orcid.org/0000-0002-0236-0806
Dirch H Petersen ⬤ https://orcid.org/0000-0002-9309-4186

References

[1] Waldrop M M 2016 The chips are down for Moore's law *Nat. News* **530** 144
[2] He J and Tritt T M 2017 Advances in thermoelectric materials research: looking back and moving forward *Science* **357** eaak9997
[3] Cahill D G *et al* 2014 Nanoscale thermal transport. II. 2003–2012 *Appl. Phys. Rev.* **1** 011305

[4] Fangohr H, Chernyshenko D S, Franchin M, Fischbacher T and Meier G 2011 Joule heating in nanowires *Phys. Rev.* B **84** 054437

[5] Lee J, Asheghi M and Goodson K E 2012 Impact of thermoelectric phenomena on phase-change memory performance metrics and scaling *Nanotechnology* **23** 205201

[6] Petersen C L, Hansen T M, Bøggild P, Boisen A, Hansen O, Hassenkam T and Grey F 2002 Scanning microscopic four-point conductivity probes *Sens. Actuators* A **96** 53–58

[7] Petersen D H *et al* 2010 Review of electrical characterization of ultra-shallow junctions with micro four-point probes *J. Vac. Sci. Technol.* B **28** C1C27

[8] Platzek D, Karpinski G, Stiewe C, Ziolkowski P, Drasar C and Muller E 2005 Potential-Seebeck-microprobe (PSM): measuring the spatial resolution of the Seebeck coefficient and the electric potential *ICT 2005. 24th Int. Conf. on Thermoelectrics, 2005* (IEEE) pp 13–16

[9] Wilson A A, Rojo M M, Abad B, Perez J A, Maiz J, Schomacker J, Martín-Gonzalez M, Borca-Tasciuc D A and Borca-Tasciuc T 2015 Thermal conductivity measurements of high and low thermal conductivity films using a scanning hot probe method in the 3ω mode and novel calibration strategies *Nanoscale* **7** 15404–12

[10] Taylor P J, Wilson A, Maddux J R, Borca-Tascuic T, Moran S P, Castillo E and Borca-Tascuic D 2018 Novel measurement methods for thermoelectric power generator materials and devices *Innov. Army Energy Power Mater. Technol.* **36** 392

[11] Riddle J L, Furukawa G T and Plumb H H 1973 *Nat. Bureau Stand.* **126**

[12] Batagelj V, Bojkovski J and Drnovšek J 2003 Methods of reducing the uncertainty of the self-heating correction of a standard platinum resistance thermometer in temperature measurements of the highest accuracy *Meas. Sci. Technol.* **14** 2151

[13] Goupil C, Seifert W, Zabrocki K, Müller E and Snyder G J 2011 Thermodynamics of thermoelectric phenomena and applications *Entropy* **13** 1481–517

[14] Serbulova K and Vountesmery Y 2019 Simulation of the sample overheat for the four point semiconductor resistivity measurement *2019 IEEE 39th Int. Conf. on Electronics and Nanotechnology (ELNANO)* (IEEE) pp 369–74

[15] Marangoni T A, Guralnik B, Borup K A, Hansen O and Petersen D H 2021 Determination of the temperature coefficient of resistance from micro four-point probe measurements *J. Appl. Phys.* **129** 165105

[16] Guralnik B *et al* 2021 3ω correction method for eliminating resistance measurement error due to Joule heating *Rev. Sci. Instrum.* **92** 094711

[17] Landau L D and Lifshitz E M 1960 *Electrodynamics of Continuous Media* (Oxford: Pergamon) § 25

[18] Cutler M 1961 Thermoelectric measurements at small-area contacts *J. Appl. Phys.* **32** 1075–82

[19] Kaganov M A and Yangarber V A 1965 The temperature field in a homogeneous medium heated by an electric current under conditions of spherical symmetry *J. Appl. Mech. Tech. Phys.* **6** 103–6

[20] Holm R 1948 Calculation of the temperature development in a contact heated in the contact surface, and application to the problem of the temperature rise in a sliding contact *J. Appl. Phys.* **19** 361–6

[21] Uhlir A Jr 1955 The potentials of infinite systems of sources and numerical solutions of problems in semiconductor engineering *Bell Syst. Tech. J.* **34** 105–28

[22] Tritt T M and Browning V M 2001 Overview of measurement and characterization techniques for thermoelectric materials *Semiconductors and Semimetals* vol 69 (Amsterdam: Elsevier) pp 25–49

[23] The Math Works Inc. MATLAB® v 2020a (Natick, MA) (available at: www.mathworks.com)

[24] COMSOL AB COMSOL Multiphysics® v. 5.6 2022 (Stockholm) (available at: www.comsol.com)

[25] Lee Y and Hwang G S 2012 Mechanism of thermal conductivity suppression in doped silicon studied with nonequilibrium molecular dynamics *Phys. Rev.* B **86** 075202

[26] Ohishi Y, Takarada S, Aikebaier Y, Muta H, Kurosaki K, Yamanaka S, Miyazaki Y, Uchida N and Tada T 2016 Thermoelectric properties of gallium-doped p-type germanium *Jpn. J. Appl. Phys.* **55** 051301

[27] Wang X Y, Yu J, Zhao R F, Zhu B, Gao N, Xiang B, Yu Y, Zhang K M, Huang Z Y and Zu F Q 2019 Effects of melting time and temperature on the microstructure and thermoelectric properties of p-type $Bi_{0.3}Sb_{1.7}Te_3$ alloy *J. Phys. Chem. Solids* **124** 281–8

[28] Hu L, Zhu T, Liu X and Zhao X 2014 Point defect engineering of high-performance bismuth-telluride-based thermoelectric materials *Adv. Funct. Mater.* **24** 5211–8

[29] Gustafsson S E 1991 Transient plane source techniques for thermal conductivity and thermal diffusivity measurements of solid materials *Rev. Sci. Instrum.* **62** 797–804

[30] Gustavsson M, Karawacki E and Gustafsson S E 1994 Thermal conductivity, thermal diffusivity, and specific heat of thin samples from transient measurements with hot disk sensors *Rev. Sci. Instrum.* **65** 3856–9

[31] He Y 2005 Rapid thermal conductivity measurement with a hot disk sensor: part 1. Theoretical considerations *Thermochim. Acta* **436** 122–9

[32] De Boor J and Müller E 2013 Data analysis for Seebeck coefficient measurements *Rev. Sci. Instrum.* **84** 065102

[33] Weiss H 1956 Bestimmung der effektiven Massen in InSb und InAs aus Messungen der differentiellen Thermospannung *Z. Nat.forsch.* A **11** 131–8

[34] Iwanaga S, Toberer E S, LaLonde A and Snyder G J 2011 A high temperature apparatus for measurement of the Seebeck coefficient *Rev. Sci. Instrum.* **82** 063905

[35] Borup K A *et al* 2015 Measuring thermoelectric transport properties of materials *Energy Environ. Sci.* **8** 423–35

[36] Henrichsen H H, Hansen O, Kjaer D, Nielsen P F, Wang F and Petersen D H 2014 Precision of single-engage micro Hall effect measurements *2014 Int. Workshop on Junction Technology (IWJT)* (IEEE) pp 1–4

[37] Cagliani A, Østerberg F W, Hansen O, Shiv L, Nielsen P F and Petersen D H 2017 Breakthrough in current-in-plane tunneling measurement precision by application of multi-variable fitting algorithm *Rev. Sci. Instrum.* **88** 095005

[38] Jaschinsky P, Wensorra J, Lepsa M I, Mysliveček J and Voigtländer B 2008 Nanoscale charge transport measurements using a double-tip scanning tunneling microscope *J. Appl. Phys.* **104** 094307

[39] Lin J Y J, Roy A M and Saraswat K C 2012 Reduction in specific contact resistivity to n+ Ge using TiO_2 interfacial layer *IEEE Electron Device Lett.* **33** 1541–3

[40] Lotz M R, Boll M, Hansen O, Kjær D, Bøggild P and Petersen D H 2014 Revealing origin of quasi-one dimensional current transport in defect rich two dimensional materials *Appl. Phys. Lett.* **105** 053115

[41] Liu Y *et al* 2018 High thermoelectric performance in crystallographically textured n-type $Bi_2Te_{3-x}Se_x$ produced from asymmetric colloidal nanocrystals *ACS Nano* **12** 7174–84

[42] Yamashita O 2004 Effect of metal electrode on Seebeck coefficient of p-and n-type Si thermoelectrics *J. Appl. Phys.* **95** 178–83

[43] Zeng L *et al* 2015 Measuring phonon mean free path distributions by probing quasiballistic phonon transport in grating nanostructures *Sci. Rep.* **5** 1–10

[44] Henry A S and Chen G 2008 Spectral phonon transport properties of silicon based on molecular dynamics simulations and lattice dynamics *J. Comput. Theor. Nanosci.* **5** 141–52

[45] Koh Y K and Cahill D G 2007 Frequency dependence of the thermal conductivity of semiconductor alloys *Phys. Rev.* B **76** 075207

[46] Regner K T, Sellan D P, Su Z, Amon C H, McGaughey A J and Malen J A 2013 Broadband phonon mean free path contributions to thermal conductivity measured using frequency domain thermoreflectance *Nat. Commun.* **4** 1–7

[47] Carrete J, Vermeersch B, Katre A, van Roekeghem A, Wang T, Madsen G K and Mingo N 2017 almaBTE: a solver of the space–time dependent Boltzmann transport equation for phonons in structured materials *Comput. Phys. Commun.* **220** 351–62

[48] Worledge D C and Trouilloud P L 2003 Magnetoresistance measurement of unpatterned magnetic tunnel junction wafers by current-in-plane tunneling *Appl. Phys. Lett.* **83** 84–86

[49] Petersen D H, Hansen O, Lin R and Nielsen P F 2008 Micro-four-point probe Hall effect measurement method *J. Appl. Phys.* **104** 013710